# Nanoscale Structure and Morphology of Atomic Layer Deposition Platinum on $SrTiO_3$ (001)

Steven T. Christensen,[†] Jeffrey W. Elam,[‡] Byeongdu Lee,[§] Zhenxing Feng,[†] Michael J. Bedzyk,[†,||] and Mark C. Hersam*[,†,⊥]

*Department of Materials Science and Engineering and Department of Chemistry, Northwestern University, Evanston, Illinois 60208, and Energy Systems Division, X-ray Science Division, and Materials Science Division, Argonne National Laboratory, Argonne, Illinois 60439*

*Received October 2, 2008. Revised Manuscript Received November 26, 2008*

The early stages of nucleation and growth of atomic layer deposition (ALD) platinum on $SrTiO_3$ (001) have been studied. Scanning electron microscopy reveals the ALD Pt deposits as discrete nanoparticles that grow and coalesce with increasing number of ALD cycles, ultimately resulting in a continuous film after ~40 cycles. Atomic force microscopy shows the films to be fine-grained and highly conformal such that the 0.4 nm atomic steps of the underlying $SrTiO_3$ (001) surface remain visible even after 80 Pt ALD cycles. Grazing-incidence small-angle X-ray scattering (GISAXS) studies demonstrate that the early stages of Pt ALD yields nanoparticles that are well approximated as cylinders with a height to radius ratio that is nearly unity. Consistent with nanoparticle coalescence, GISAXS also reveals an interparticle spacing that increases with the number of ALD cycles. X-ray fluorescence measurements of the Pt coverage reveal growth dynamics in which the Pt deposition is initially faster than the steady-state growth rate that emerges after 40−70 ALD cycles. These experimental results are understood through the application of a model that suggests that the $SrTiO_3$ surface is more reactive than the Pt species and that Pt diffusion is operative in nanoparticle formation. Overall, this study delineates ALD growth conditions for forming either Pt nanoparticles or continuous Pt thin films on $SrTiO_3$ (001), thus presenting potentially useful substrates for catalysis and microelectronics, respectively.

## Introduction

Strontium titanate has a broad range of technological applications including insulating layers in dynamic random access memory and field effect transistors, ferroelectric devices, and catalysts.[1−7] In many of these applications, it is advantageous to couple the $SrTiO_3$ to platinum layers to serve as electrodes for microelectronic devices or to increase the chemical activity of catalysts. In particular, it is critical to control the Pt morphology to obtain either a smooth, flat surface for microelectronic electrodes or small, highly dispersed nanoparticles for catalysis.

Atomic layer deposition (ALD) is a thin film growth technology that utilizes alternating, self-limiting exposures between a solid surface and gaseous precursors to deposit materials in an atomic layer-by-layer fashion.[8,9] ALD allows for precise control over both thickness and composition and allows complex, three-dimensional surfaces such as deep trenches or nanoporous templates to be coated with nearly ideal conformality. Furthermore, the early stages of ALD growth can lead to the nucleation of nanoparticles.[10−16] These attributes make ALD an attractive technology for preparing both the films and nanoparticles mentioned above.

In this study, we deposit Pt on $SrTiO_3$ (001) with ALD using alternating exposures to (Trimethyl)methylcyclopentadienylplatinum (IV) ($MeCpPtMe_3$) and oxygen. Previous studies of Pt ALD using these precursors have focused mainly on the thick-film limit in which Pt is deposited on

* Corresponding author. E-mail: m-hersam@northwestern.edu.
[†] Department of Materials Science and Engineering, Northwestern University.
[‡] Energy Systems Division, Argonne National Laboratory.
[§] X-ray Science Division, Argonne National Laboratory.
[||] Materials Science Division, Argonne National Laboratory.
[⊥] Department of Chemistry, Northwestern University.

(1) Baldus, O.; Waser, R. *Appl. Phys. A: Mater. Sci. Process.* **2005**, *80* (7), 1553–1562.
(2) Marti, X.; Sanchez, F.; Hrabovsky, D.; Fontcuberta, J.; Laukhin, V.; Skumryev, V.; Garcia-Cuenca, M. V.; Ferrater, C.; Varela, M.; Luders, U.; Bobo, J. F.; Estrade, S.; Arbiol, J.; Peiro, F. *J. Cryst. Growth* **2007**, *299* (2), 288–294.
(3) Schmidt, S.; Ok, Y. W.; Klenov, D. O.; Lu, J. W.; Keane, S. P.; Stemmer, S. *J. Mater. Res.* **2005**, *20* (9), 2261–2265.
(4) Wagner, F. T.; Ferrer, S.; Somorjai, G. A. *Surf. Sci.* **1980**, *101* (1−3), 462–474.
(5) Wagner, F. T.; Somorjai, G. A. *J. Am. Chem. Soc.* **1980**, *102* (17), 5494–5502.
(6) Carr, R. G.; Somorjai, G. A. *Nature* **1981**, *290* (5807), 576–577.
(7) Wagner, F. T.; Somorjai, G. A. *Nature* **1980**, *285* (5766), 559–560.
(8) Ritala, M. *Appl. Surf. Sci.* **1997**, *112*, 223–230.
(9) Suntola, T. *Thin Solid Films* **1992**, *216* (1), 84–89.
(10) Aaltonen, T.; Ritala, M.; Sajavaara, T.; Keinonen, J.; Leskela, M. *Chem. Mater.* **2003**, *15* (9), 1924–1928.
(11) Aaltonen, T.; Ritala, M.; Tung, Y. L.; Chi, Y.; Arstila, K.; Meinander, K.; Leskela, M. *J. Mater. Res.* **2004**, *19* (11), 3353–3358.
(12) Zhu, Y.; Dunn, K. A.; Kaloyeros, A. E. *J. Mater. Res.* **2007**, *22* (5), 1292–1298.
(13) Elam, J. W.; Libera, J. A.; Pellin, M. J.; Zinovev, A. V.; Greene, J. P.; Nolen, J. A. *Appl. Phys. Lett.* **2006**, *89* (5), 053124.
(14) Elam, J. W.; Zinovev, A.; Han, C. Y.; Wang, H. H.; Welp, U.; Hryn, J. N.; Pellin, M. J. *Thin Solid Films* **2006**, *515* (4), 1664–1673.
(15) Johansson, A.; Lu, J.; Carlsson, J. O.; Boman, M. *J. Appl. Phys.* **2004**, *96* (9), 5189–5194.
(16) King, J. S.; Wittstock, A.; Biener, J.; Kucheyev, S. O.; Wang, Y. M.; Baumann, T. F.; Giri, S. K.; Hamza, A. V.; Baeumer, M.; Bent, S. F. *Nano Lett.* **2008**, *8* (8), 2405–2409.

10.1021/cm8026863 CCC: $40.75 © 2009 American Chemical Society
Published on Web 01/02/2009

itself.[10−12,17] These studies support a Pt ALD mechanism in which adsorbed oxygen on the Pt surface plays a critical role by providing reactive sites for the $MeCpPtMe_3$ precursor. On the other hand, Pt ALD on $SrTiO_3$ (001) is likely to possess a more complex growth mechanism due to differences in the surface chemistry between the initial $SrTiO_3$ (001) substrate and the growing Pt film. Of particular interest is the initial nucleation process on the $SrTiO_3$ (001) surface because it will likely dictate the morphology of the Pt deposit. Our previous work demonstrated that the substrate chemistry can strongly influence the initial nucleation during Pt ALD.[18]

Here, we concentrate on characterizing the early stages of Pt ALD on $SrTiO_3$ (001) using a suite of X-ray and imaging techniques. Scanning electron microscopy (SEM) reveals that the growth mechanism begins with the nucleation of Pt nanoparticles on the bare $SrTiO_3$ (001) surface. During subsequent growth, the Pt nanoparticles conformally coat the surface such that the 0.4 nm atomic steps of the underlying $SrTiO_3$ (001) substrate remain observable with atomic force microscopy (AFM) for up to 80 ALD cycles. With the aid of SEM and AFM, nanoparticle coalescence leading to a continuous Pt film is identified at ∼40 ALD cycles. Using grazing-incidence small-angle X-ray scattering (GISAXS), the ensemble average nanoparticle dimensions and interparticle spacing are further quantified. In addition, through X-ray fluorescence (XRF) characterization, the Pt ALD growth rate is measured and found to undergo a discontinuous transition upon formation of a continuous film. These experimental observations are understood by applying a model that includes a combination of increased number of reactive sites on the $SrTiO_3$ (001) surface and Pt surface diffusion playing a role in nanoparticle formation. These results can likely be applied to the early stages of ALD growth for other noble metals such as palladium and ruthenium.

## Experimental Details

**Substrate Preparation.** 10 mm × 10 mm × 1 mm $SrTiO_3$ (001) substrates (MTI Corp.) were ultrasonically degreased for 5 min in acetone and isopropanol. The substrates were then sonicated in deionized water (18 MΩ/cm) for 15 min and subsequently etched in a hydrofluoric acid/ammonium fluoride solution (Riddel-de Haen part no. 40207, pH ∼5) for approximately 45 s. The substrates were then rinsed in deionized water and dried with filtered $N_2$. After etching, the substrates were loaded into a tube furnace with flowing $O_2$ (∼100 sccm) and annealed at 1050 °C for 5 h. This treatment produces a surface of clean, atomically flat terraces with 0.4 nm step heights, which is consistent with the $SrTiO_3$ lattice constant of 0.3905 nm.

**Atomic Layer Deposition.** The $SrTiO_3$ (001) substrates were transferred to a custom ALD reactor consisting of a hot-walled stainless steel tube and a computer controlled gas manifold for precursor dosing.[19] After installing the $SrTiO_3$ substrates in the ALD reactor, the substrates were allowed to equilibrate and outgas for 10 min at 300 °C in flowing nitrogen before commencing the Pt ALD. Platinum ALD was accomplished using alternating exposures to $MeCpPtMe_3$ (Strem Chemicals, 99.5% pure) and 400 sccm of ultrahigh purity (99.995% pure) oxygen at 300 °C using 360 sccm of ultrahigh purity (99.995% pure) nitrogen carrier gas at a steady state pressure of ∼1 Torr. During the $MeCpPtMe_3$ exposures, 300 sccm of $N_2$ was passed through a stainless steel bubbler containing the $MeCpPtMe_3$ heated to 40 °C, and the $N_2$ was diverted to bypass the bubbler after the exposures. Each Pt ALD cycle consisted of a 10 s exposure to $MeCpPtMe_3$, a 5 s $N_2$ purge period, a 5 s exposure to $O_2$, and a final 5 s $N_2$ purge period. Companion ellipsometry and quartz crystal microbalance measurements on silicon substrates yielded a growth rate of 0.5 Å/cycle Pt (see the Supporting Information, Figure S1). X-ray photoelectron spectroscopy measurements on ALD Pt/$SrTiO_3$ (001) substrates confirmed that the platinum chemical state is metallic, which is consistent with previous reports using these precursors (see the Supporting Information, Figure S2).[10−12,17,20]

**Atomic Force Microscopy.** AFM images were collected in open air using a Thermomicroscopes CP Research AFM operated in intermittent contact mode. The silicon AFM tips ($\mu$Masch) possessed a nominal 10 nm radius of curvature and resonant frequency of ∼70 kHz. A polynomial subtraction was applied to the images to correct for piezo tube motion. The vertical piezo response was calibrated with the atomic steps of $SrTiO_3$ (001) and $TiO_2$ (110).

**Grazing-Incidence Small-Angle X-ray Scattering.** Synchrotron X-ray studies were performed at the Advanced Photon Source (Argonne National Laboratory, Argonne, Illinois) at the 12ID beam line. GISAXS measurements were performed at an incident photon energy of 8.00 keV. The samples were mounted on a two-circle diffractometer that enabled rotations to set the incident angle, $\alpha_i$, and rotation about the substrate surface normal, $\phi$. The data were collected using a 2048 by 2048 pixel MAR165 CCD detector with a detector to sample distance of 2.1 m. Detector oversaturation was avoided by using a tungsten beam stop. Calibration was achieved with a silver behenate standard, and images were corrected for detector dark current via data subtraction.

**X-ray Fluorescence.** The incident X-ray beam for the XRF measurements was generated with a modified rotating anode target that consisted of ∼6 $\mu$m Zr metal sputtered onto a Cr base. The 15.75 keV K$\alpha$ radiation from the Zr coating made it possible to excite Pt L$\alpha$ fluorescence while avoiding excitation of an intense Sr K$\alpha$ fluorescence from the $SrTiO_3$ substrate that would have saturated the Vortex silicon-drift-diode fluorescence detector (SII NanoTechnology). The rotating anode line source was operated at 40 kV and 140 mA. The incident beam was conditioned with a graded parabolic multilayer optic (Osmic) and defined by a 0.5 mm by 2 mm incident beam slit leading to an incident flux of ∼$1 \times 10^7$ photons/s. The Pt L$\alpha$ XRF yield from each ALD deposited film was converted into a Pt coverage by a side-by-side comparison to a Pt standard for which the Pt areal density had been calibrated by Rutherford backscattering.

## Results

Following chemical etching and oxygen annealing, the AFM image of Figure 1 reveals atomically flat terraces with 0.4 nm steps. Clean atomic terraces are useful for imaging nanoparticles and films since they provide a vertically calibrated and flat backdrop to measure heights and roughness. Figure 2 illustrates the evolution of Pt film growth with AFM images after 10, 15, 20, and 80 ALD cycles. For Pt/$SrTiO_3$ samples prepared using 15 or fewer ALD cycles, only

(17) Aaltonen, T.; Rahtu, A.; Ritala, M.; Leskela, M. *Electrochem. Solid-State Lett.* **2003**, *6* (9), C130–C133.
(18) Elam, J. W.; Zinovev, A. V.; Pellin, M. J.; Comstock, D. J.; Hersam, M. C. *ECS Trans.* **2006**, *3* (15), 271–278.
(19) Elam, J. W.; Groner, M. D.; George, S. M. *Rev. Sci. Instrum.* **2002**, *73* (8), 2981–2987.
(20) Hiratani, M.; Nabatame, T.; Matsui, Y.; Imagawa, K.; Kimura, S. *J. Electrochem. Soc.* **2001**, *148* (8), C524–C527.

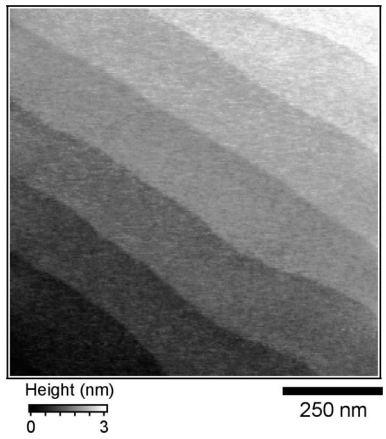


**Figure 1.** AFM image of the $SrTiO_3$ (001) substrate following chemical etching and annealing in oxygen. Atomically flat terraces with 0.4 nm step heights are clearly visible. Stepped surfaces provide a useful backdrop to monitor the morphology of growing films with respect to a particular orientation of a single-crystal surface.

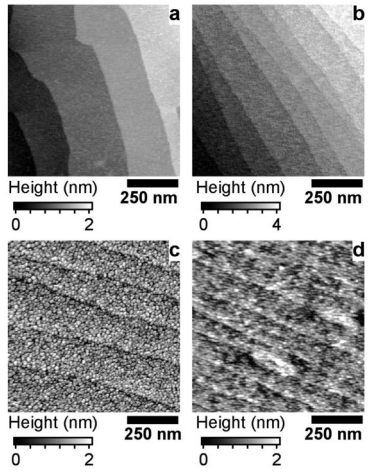


**Figure 2.** AFM images following Pt ALD: (a) 10, (b) 15, (c) 20, (d) 80 ALD cycles. At 20 ALD cycles, Pt nanoparticles can be directly observed, whereas the Pt film possesses a fine granular structure after 80 ALD cycles. The 0.4 nm atomic steps of the underlying $SrTiO_3$ (001) substrate can still be observed after 80 ALD cycles.

subtle changes can be perceived in AFM. After 20 ALD cycles, Pt nanoparticles appear to be decorating the surface, whereas a granular, continuous Pt film is apparent following 80 ALD cycles. The AFM data also show that the 0.4 nm atomic steps of the underlying $SrTiO_3$ (001) substrate are still observable, even in the case of 80 ALD cycles.

Figure 3 presents SEM images following 15, 20, 30, 40, and 80 Pt ALD cycles. These images clearly show that the Pt nucleates on the $SrTiO_3$ surface as discrete islands that grow laterally with increasing ALD cycles. The lateral spacing of these nanoparticles is on the order of a few nanometers. The nanoparticles coalesce to form a nearly continuous film at approximately 40 ALD cycles as evident in the morphology and the decreasing number of isolated nanoparticles per area. Evidence for persistent $SrTiO_3$ (001) step edges are also apparent as indicated by the diagonal line cutting across Figure 3b.

Grazing incidence small-angle X-ray scattering provides a quantitative means to study the ensemble average morphology and structure of the Pt ALD films. Figure 4 provides a schematic of the GISAXS setup and scattering data for a blank $SrTiO_3$ substrate after being etched and annealed. Figure 4a geometrically defines the scattering vector, **q**, which represents the momentum transfer of the incident ($\mathbf{k}_i$) and scattered ($\mathbf{k}_f$) wave vectors where: $\mathbf{q} = \mathbf{k}_f - \mathbf{k}_i$. The Cartesian definition of **q** is given by

$$q_x = k_0[\cos(2\theta_f)\cos(\alpha_f) - \cos(\alpha_i)],$$
$$q_y = k_0\sin(2\theta_f)\cos(\alpha_f),$$
$$q_z = k_0[\sin(\alpha_f) + \sin(\alpha_i)]$$
$$q_{xy} = q_{\parallel} = \sqrt{q_x^2 + q_y^2}, \quad (1)$$

where $k_0 = 2\pi/\lambda$ with $\lambda$ being the X-ray wavelength.

Two-dimensional GISAXS data are presented in Figure 5 for 10, 20, 30, and 40 cycles of Pt ALD. The scattering intensity concentrates in the small angle region as the number of ALD cycles increases, thus indicating that the Pt nanoparticles are increasing in size. Also, the GISAXS peak representative of interparticle spacing becomes more apparent as the number of ALD cycles increases. Line cuts of intensity

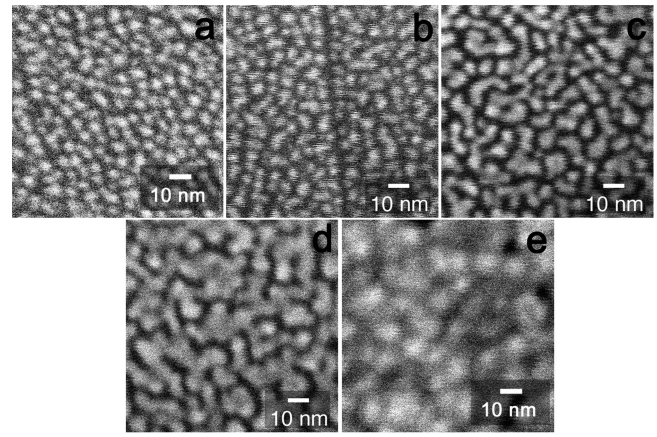


**Figure 3.** SEM images following Pt ALD: (a) 15, (b) 20, (c) 30, (d) 40, (e) 80 cycles. At 15 ALD cycles, Pt nanoparticles have nucleated and then grow and coalesce with increasing ALD cycles. Film closure occurs at ~40 ALD cycles.

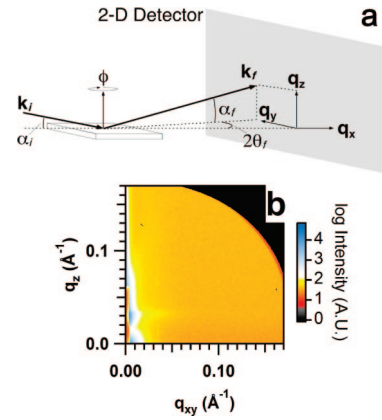


**Figure 4.** GISAXS data collection: (a) schematic of the GISAXS experimental geometry and (b) GISAXS scattering data for a blank $SrTiO_3$ (001) substrate after etching and annealing. The vectors and angles given in (a) provide the basis for defining the momentum transfer, $q$, of the scattering process according to eq 1. The CCD area detector captures the typical GISAXS data for the blank substrate in (b), where intensity is due primarily to X-rays reflected off the surface.

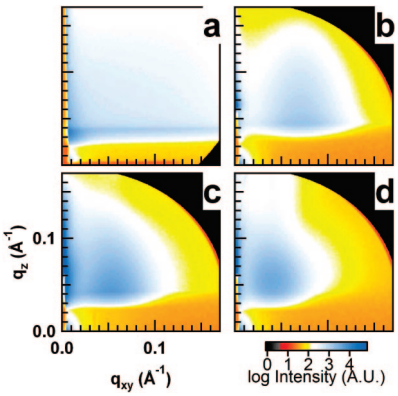


**Figure 5.** GISAXS data after (a) 10, (b) 20, (c) 30, (d) 40 ALD cycles. The scattering from the coalescing Pt film creates lobes of intensity captured in the CCD image. The scattered intensity lobe moves inward as the number of ALD cycles increases, thus indicating that the particle size and the interparticle spacing (center-to-center) are increasing.

versus $q$ were extracted from the two-dimensional GISAXS data and fit using the distorted wave Born approximation[21,22] (DWBA) framework with a cylinder form factor and an interference function under local monodisperse approximation[21,23] (LMA). In addition, the 1D paracrystal model[21,24] was used to represent the interparticle spacing distribution. The vertical data was fit using the IsGISAXS software.[21] The general intensity is given by

$$I(\mathbf{q}) = \langle |F(\mathbf{q})|^2 \rangle S(\mathbf{q}) \tag{2}$$

where $\langle |F(\mathbf{q})|^2 \rangle$ is the average form factor that describes the nanoparticle shape and size, and $S(\mathbf{q})$ is the interference function that yields the interparticle spacing. The line cut data and fits are plotted in Figure 6.

For the in-plane scattering, an additional term was added to the scattered intensity in eq 2 in order to account for strong scattering near $q_{xy} = 0$. This term is based on the unified model from Beaucage[25,26] to give the lateral scattering intensity, $I(q_{xy})$, as

$$I(q_{xy}) = I_U(q_{xy}) + \langle |F(q_{xy})|^2 \rangle S(q_{xy}) \tag{3}$$

where $I_U(q_{xy})$ is determined by the unified model, and $\langle |F(q_{xy})|^2 \rangle S(q_{xy})$ represents the particle scattering for the DWBA with the LMA. The general form of the intensity from the unified model is calculated as:

$$I_U(q) = G\exp\left(-\frac{q^2 R_g^2}{3}\right) + B\left(\frac{1}{q}\right)^P \tag{4}$$

The parameters related to $I_U(q_{xy})$ include the Guinier prefactor, $G$, the Guinier radius, $R_g$, the power-law prefactor, $B$, and the power-law exponent, $P$. The fitting results including the unified model parameters and particle dimension and spacing are summarized in Table 1.

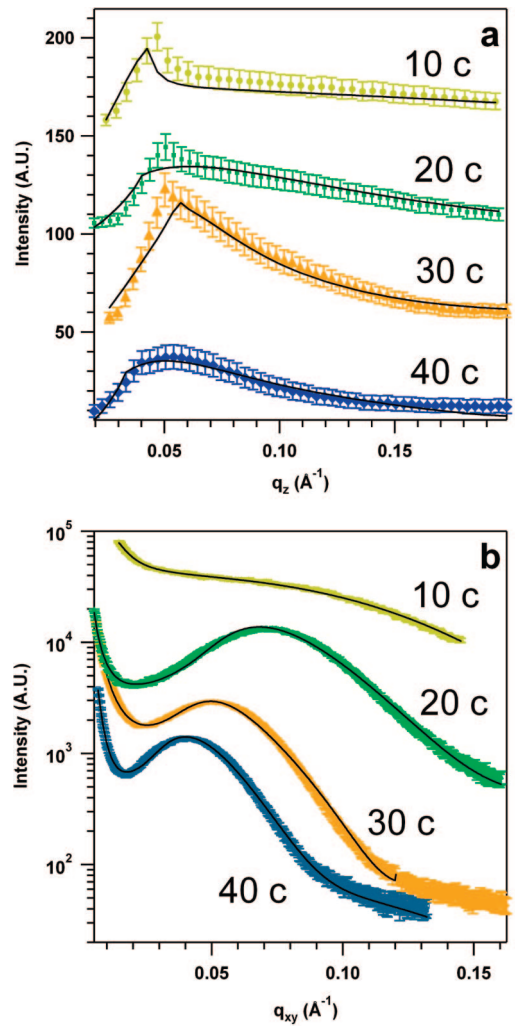


**Figure 6.** GISAXS line cut data and fits for (a) vertical and (b) horizontal scattering. The individual curves are offset for clarity. The line cuts are taken along the horizontal and vertical scattering planes of the data in the CCD images. These data were fit with a distorted wave Born approximation cylinder form factor and the local monodisperse approximation to extract the Pt nanoparticle size and spacing. The horizontal fitting also included a term based on the unified small-angle X-ray scattering model that accounts for the data near the beam stop.

The fitting results from Table 1 confirm the observations from the microscopy data that the in-plane particle size, $R$, increases from 1.1 to 3.5 nm with increasing number of Pt ALD cycles. The GISAXS data also reveal that the out-of-plane particle size, $H$, increases from 1.2 to 3.8 nm. The $H/R$ aspect ratio for all particles is nearly unity, which indicates that the Pt nanoparticles grow isotropically under these conditions. The interparticle spacing, $D$, is defined as the center-to-center distance for the Pt nanoparticles. From the GISAXS results, the interparticle spacing is found to increase from 2.4 to 9.0 nm, which is consistent with nanoparticle coalescence causing a decrease in the number of particles per unit area.

XRF measurements allow the Pt surface coverage to be measured as a function of the number of ALD cycles as displayed in Figure 7. This plot suggests a decrease in the growth rate following ~40 ALD cycles. The solid line plotted in Figure 7 results from the growth model that is discussed below.

(21) Lazzari, R. *J. Appl. Crystallogr.* **2002**, *35*, 406–421.
(22) Rauscher, M.; Salditt, T.; Spohn, H. *Phys. Rev. B* **1995**, *52* (23), 16855–16863.
(23) Pedersen, J. S. *J. Appl. Crystallogr.* **1994**, *27*, 595–608.
(24) Hosemann, R.; Bagchi, S. N., *Direct Analysis of Matter by Diffraction*; North-Holland: Amsterdam, 1962.
(25) Beaucage, G. *J. Appl. Crystallogr.* **1995**, *28*, 717–728.
(26) Beaucage, G. *J. Appl. Crystallogr.* **1996**, *29*, 134–146.

**Table 1. GISAXS Fitting and Analysis Results**[a]

| ALD cycles | $R$ (nm) | $\sigma_R$ (nm) | $H$ (nm) | $\sigma_H$ (nm) | H/R | $D$ (nm) | $\sigma_D$ (nm) | $G$ | $R_g$ (nm) | $B$ | $P$ |
|---|---|---|---|---|---|---|---|---|---|---|---|
| 10 | 1.1 | 0.1 | 1.2 | 0.3 | 1.1 | 2.2 | 0.8 | $8.7 \times 10^7$ | 35 | $1.4 \times 10^2$ | 3.8 |
| 20 | 2.1 | 0.5 | 2.3 | 0.6 | 1.1 | 6.3 | 1.3 | $3.0 \times 10^1$ | 54 | $2.9 \times 10^3$ | 2.4 |
| 30 | 3.1 | 0.7 | 3.0 | 0.8 | 1.0 | 9.0 | 2.1 | $7.8 \times 10^4$ | 31 | $3.1 \times 10^3$ | 2.4 |
| 40 | 3.5 | 0.9 | 3.8 | 1.0 | 1.1 | 9.0 | 2.5 | $2.0 \times 10^5$ | 90 | $2.9 \times 10^2$ | 3.6 |

[a] GISAXS fitting and analysis results. The particle model is taken to be a cylinder of radius, $R$, and height, $H$, with a center-to-center interparticle spacing, $D$, $G$, $R_g$, $B$, and $P$ are parameters from the unified fit model for scattering near the beamstop. The $\sigma$ parameter gives the distribution width of the respective parameters.

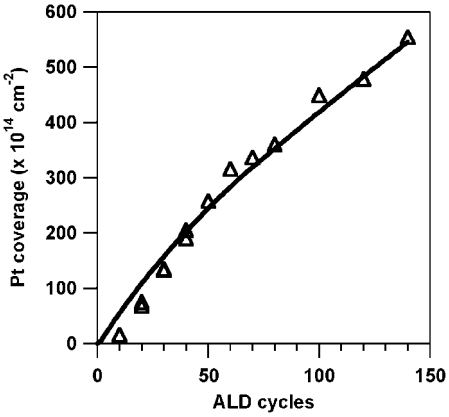


**Figure 7.** XRF Pt coverage versus ALD cycle. The XRF measures the number of platinum atoms deposited per ALD cycle. A change in growth rate is observed at ~40 ALD cycles corresponding to film closure. Prior to 40 ALD cycles, the growth rate is approximately double the steady-state growth rate reported in the literature, which is reflected in the data above 40 cycles. The solid line is based on a growth model that accounts for more reactive sites on bare $SrTiO_3$ than Pt.

## Discussion

The model for Pt ALD proposed by Aaltonen et al. asserts that oxygen adsorbed on the surface of the Pt film dissociates the $MeCpPtMe_3$ precursor during the metal-organic exposures.[10] Consequently, we expect that any Pt present on the $SrTiO_3$ from the initial Pt ALD cycles will provide reactive sites for $MeCpPtMe_3$ dissociation during subsequent Pt ALD cycles, thus leading to nanoparticle growth. However, the Aaltonen model does not address the possible influence of the bare $SrTiO_3$ surface during the Pt nucleation. Some intriguing issues lie in determining the role bare $SrTiO_3$ oxide plays in the deposition and how surface diffusion of Pt atoms may affect the growth of Pt nanoparticles on the surface prior to film closure.

Inspection of the SEM images from Figure 3 reveals that the nanoparticles for 15 cycles are relatively uniform in shape but as the number of cycles increase, elongated and nonsymmetric particle shapes appear. The nanoparticles, however, possess a narrow enough height distribution and low enough roughness that the influence of the 0.4 nm atomic steps of the underlying $SrTiO_3$ substrate remains observable in AFM for as many as 80 ALD cycles. These observations provide initial evidence for a growth mechanism that includes adsorption of $MeCpPtMe_3$ on the $SrTiO_3$ surface followed by diffusion of the Pt species to the growing nanoparticles.

Additional insight into the growth mechanism can be gained by considering the XRF data plotted in Figure 7. Specifically, Figure 7 shows two regions of growth such that the region below ~40 ALD cycles shows a growth per cycle that is approximately 2-fold higher than the region above ~40 ALD cycles. Moreover, the magnitude of the Pt growth beyond 40 ALD cycles is consistent with the previously observed growth rate for Pt ALD indicating that below 40 ALD cycles the Pt growth rate is abnormally large. The 40 ALD cycle transition point between these two growth regions coincides approximately with the point at which the ALD Pt nanoparticles coalesce to form a continuous film as observed by SEM in Figure 3c.

The region of higher initial growth is uncommon and thus requires further discussion. Existing models for nucleation and growth of ALD films[27,28] predict three growth regimes: (1) an incubation period of slow, inhibited growth; (2) a transition regime characterized by island growth and coalescence where the increasing surface area produces a nonlinear thickness change and the growth rate may exceed the steady-state growth rate by as much as 30%; (3) a steady-state regime where the thickness increases linearly. In contrast, Figure 7 exhibits an initial regime of linear growth that exceeds the steady-state growth rate by 100%, followed by a steady-state regime. To account for the initial regime of higher, linear growth observed here, we modified the existing ALD growth models to one in which the Pt deposits at a higher rate on the bare $SrTiO_3$ surface, but then diffuses to the growing Pt nanoparticles. The model assumes platinum also grows on the nanoparticles, but at a lower rate. During the model film growth, the relative proportions of bare $SrTiO_3$- and Pt-coated surface are computed. At the point of nanoparticle coalescence, the platinum ALD will continue only on the platinum film because there is no more bare $SrTiO_3$ substrate available. In this model, the distance between the nanoparticles, as well as the fraction of reactive sites on both the $SrTiO_3$ and the Pt, was varied to match the experimental data. It should be noted that this study did consider ALD for fewer than 10 cycles. The results (AFM and XRF) showed minimal deposition and were sporadic. This irregular deposition prevented a systematic study for fewer than 10 Pt ALD cycles.

The resulting fit is shown as the solid line in Figure 7. The fit uses an initial nanoparticle spacing of 12 nm, and the fraction of reactive sites on $SrTiO_3$ and Pt are 0.4 and 0.11, respectively. The interparticle spacing from the model agrees reasonably well with the spacing between the Pt nanoparticles in the SEM images shown in Figure 3. The fraction of reactive sites of 0.11 on the Pt reproduces the experimentally determined Pt growth rate in this study as well as from the literature.[10] The fraction of reactive sites on the $SrTiO_3$ of 0.4 suggests that the $SrTiO_3$

(27) Nilsen, O.; Karlsen, O. B.; Kjekshus, A.; Fjellvag, H. *Thin Solid Films* **2007**, *515* (11), 4527–4537.
(28) Puurunen, R. L.; Vandervorst, W. *J. Appl. Phys.* **2004**, *96* (12), 7686–7695.
(29) Gjostein, N. A. *Surfaces and Interfaces*; Burke, J. J., Reed, N. L., Weiss, V., Eds.; Syracuse University Press: Syracuse, NY, 1967.

has a density of reactive sites for Pt ALD that is approximately 4-fold higher than Pt.

This model for Pt nucleation and growth requires relatively fast diffusion of the Pt on the $SrTiO_3$ surface so that the Pt deposited on the bare $SrTiO_3$ can migrate to the Pt nanoparticles. Platinum diffusion rates on metal surfaces can be estimated by calculating the surface diffusion coefficient, $D_s$, using an empirical relationship given by Gjostein[29]

$$D_s(T) = 0.014\exp\left(-\frac{13T_m}{R_cT}\right) \quad (5)$$

Where $T$ and $T_m$ are the substrate temperature and melting point, respectively, in K, and $R_c$ is the gas constant in cal $mol^{-1}$ $K^{-1}$. At the deposition temperature, 573K, $D_s = 1.2 \times 10^{-12}$ $cm^2/s$, which for the 10 s time interval following the beginning of the oxygen exposure yields a platinum diffusion distance $x = (D_st)^{1/2} = 30$ nm. Because the SEM and GISAXS data suggest that the interparticle distance is significantly less than 30 nm, it is plausible that Pt surface diffusion will play an important role in the growth mechanism.

The increased growth rate prior to film closure shown in Figure 7 argues that the $SrTiO_3$ has a catalytic effect in the Pt ALD process. This effect is reflected in the modeling as a higher fraction of reactive sites on $SrTiO_3$ than on Pt. As a catalyst support, $SrTiO_3$ can reduce carbonaceous build up during hydrocarbon oxidation.[30−33] The implication for ALD would presumably be that the $SrTiO_3$ catalyzes the conversion of the organic ligands on the adsorbed MeCpPt-$Me_3$, thereby reducing steric hindrance and increasing the Pt growth rate.

The nucleation of most noble metals (including platinum, ruthenium, and palladium) during ALD also appears to occur via the coalescence of nanoparticles.[10−15,17] Thus, the role of diffusion is also likely to be important in the growth dynamics of these materials via ALD. For instance, nanoparticle size and number density may vary when noble metal ALD is performed on different substrates depending on the relative surface diffusion rates for these substrate materials. This hypothesis should motivate future studies directed at the early stages of noble metal growth by ALD.

## Conclusions

In summary, we have studied the early stages of nucleation and growth of ALD Pt on single crystal $SrTiO_3$ (001) surfaces. Uniformly sized Pt nanoparticles initially nucleate and then grow and coalesce into a continuous Pt film. Despite the particulate nature of the Pt nucleation, the films remain sufficiently smooth to preserve the 0.4 nm atomic steps of the underlying $SrTiO_3$ (001) substrate even after 80 ALD cycles. Using AFM, SEM, GISAXS, and XRF, we have developed a detailed growth model where Pt nanoparticles nucleate on the substrate and subsequently grow from a combination of precursor adsorption directly on the Pt nanoparticles as well as precursor adsorption on the surrounding $SrTiO_3$ followed by surface diffusion to the nanoparticles. The implications of this growth mechanism include that $SrTiO_3$ may act to catalyze the ALD precursors to produce an accelerated growth rate prior to film closure.

**Acknowledgment.** This work was supported by the Institute for Catalysis in Energy Processes, Northwestern University (U.S. Department of Energy Grant DE-FG02-03ER15457). The X-ray measurements performed at the Advanced Photon Source, Sector 12 (BESSRC), and the electron microscopy performed at the Electron Microscopy Center for Materials Research were supported at Argonne National Laboratory by the U.S. Department of Energy under Contract DE-AC02-06CH11357 to U Chicago Argonne, LLC. This work made use of Northwestern University Central Facilities supported by the Materials Research Science and Engineering Center through National Science Foundation Contract DMR-0520513. The authors are also thankful to Robin Koshy, Michael Graham, and Jerrold Carsello at NU for converting a Cr rotating anode X-ray target into a Zr target by sputter deposition.

**Supporting Information Available:** Ellipsometry, quartz crystal microbalance, and X-ray photoelectron spectroscopy data (PDF). This material is available free of charge via the Internet at http://pubs.acs.org.

CM8026863

(30) Takehira, K.; Shishido, T.; Kondo, M. *J. Catal.* **2002**, *207* (2), 307–316.
(31) Urasaki, K.; Fukuda, Y.; Sekine, Y.; Matsukata, M.; Kikuchi, E. *J. Jpn. Pet. Inst.* **2008**, *51* (2), 83–87.
(32) Urasaki, K.; Sekine, Y.; Kawabe, S.; Kikuchi, E.; Matsukata, M. *Appl. Catal., A* **2005**, *286* (1), 23–29.
(33) Urasaki, K.; Tokunaga, K.; Sekine, Y.; Kikuchi, E.; Matsukata, M. *Chem. Lett.* **2005**, *34* (5), 668–669.